

Sub-Airy Confocal Adaptive Optics Scanning Ophthalmoscopy

Nripun Sredar¹, Oladipo E. Fagbemi², and Alfredo Dubra¹

¹ Byers Eye Institute, Stanford University, Palo Alto, CA, USA

² Medical College of Wisconsin, WI, USA

Correspondence: Alfredo Dubra, Byers Eye Institute, Stanford University, Palo Alto, CA 94303, USA. e-mail: adubra@stanford.edu

Received: 13 June 2017

Accepted: 18 February 2018

Published: 4 April 2018

Keywords: adaptive optics; retinal imaging; confocal; ophthalmoscopy

Citation: Sredar N, Fagbemi OE, Dubra A. Sub-Airy confocal adaptive optics scanning ophthalmoscopy. *Trans Vis Sci Tech.* 2018;7(2):17, <https://doi.org/10.1167/tvst.7.2.17> Copyright 2018 The Authors

Purpose: To demonstrate the viability of improving transverse image resolution in reflectance scanning adaptive optics ophthalmoscopy using sub-Airy disk confocal detection.

Methods: The foveal cone mosaic was imaged in five human subjects free of known eye disease using two custom adaptive optics scanning light ophthalmoscopes (AOSLOs) in reflectance with 7.75 and 4.30 mm pupil diameters. Confocal pinholes of 0.5, 0.6, 0.8, and 1.0 Airy disk diameters (ADDs) were used in a retinal conjugate plane before the light detector. Average cone photoreceptor intensity profile width and power spectrum were calculated for the resulting images. Detected energy using a model eye was recorded for each pinhole size.

Results: The cone photoreceptor mosaic is better resolved with decreasing confocal pinhole size, with the high spatial frequency content of the images enhanced in both the large- and small-pupil AOSLOs. The average cone intensity profile width was reduced by ~15% with the use of a 0.5 ADD pinhole when compared to a 1.0 ADD, with an accompanying reduction in signal greater than a factor of four.

Conclusions: The use of sub-Airy disk confocal pinhole detection without increasing retinal light exposure results in a substantial improvement in image resolution at the cost of larger than predicted signal reduction.

Translational Relevance: Improvement in transverse resolution using sub-Airy disk confocal detection is a practical and low-cost approach that is applicable to all point- and line-scanning ophthalmoscopes, including optical coherence tomographers.

Introduction

Advances in ophthalmic imaging technologies^{1–3} beyond the fundus camera^{4,5} have improved our ability to noninvasively study the human retina, diagnose eye disease, and monitor the impact of treatment.⁶ In particular, the use of confocal detection in scanning ophthalmoscopes provide increased contrast through axial sectioning.^{7,8} A less-exploited advantage of confocal ophthalmoscopy is that transverse resolution can be improved by up to ~20% when the effective size of the confocal pinhole that spatially filters light before reaching the light detector is reduced to about one half of the Airy disk⁹ in the absence of monochromatic aberrations.

Confocal point-scanning ophthalmoscopes enhanced with adaptive optics (AO) correction of the

ocular monochromatic aberrations^{10,11} enable resolution of subcellular retinal structures¹² through the use of large (>3 mm) pupils. Refinements of reflective AO ophthalmoscope optical design^{13–15} and correction of non-common path aberrations^{16–18} have been demonstrated, seeking to improve resolution to the classical diffraction limit. Two additional approaches, well known in microscopy, have been demonstrated to go beyond this limit. The first approach is the use of annular pupils,^{19–21} and the second is the use of sub-Airy confocal detection,⁹ which is the topic of this work. Annular illumination pupil results in improved transverse resolution at the expense of extended depth of focus, also changing the cone photoreceptor intensity profile from point-like to more complex shapes that correspond to higher spatial modes that result from their wave-guiding properties. Prior

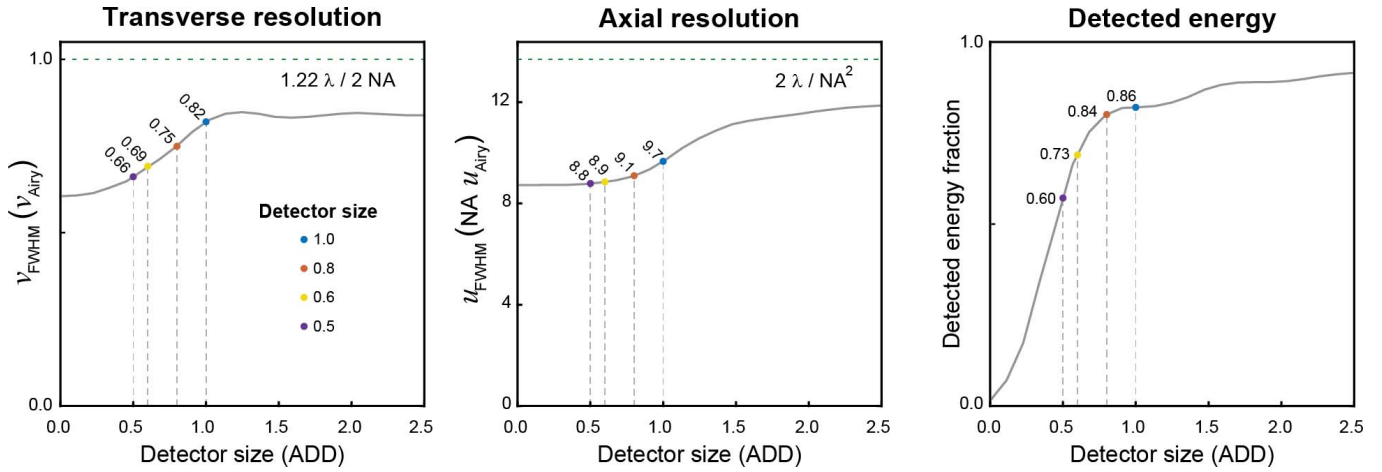


Figure 1. Theoretical confocal scanning microscope/ophthalmoscope transverse resolution (*left*), axial resolution (*center*), and detected energy (*right*) as functions of the confocal pinhole size in ADD units. The vertical axes of the left and center plots are in units of the dimensionless radial and axial microscopy coordinates, respectively.^{19,21} The *horizontal dashed lines* on the resolution plots show the first minima of the PSF of an aberration-free rotationally symmetric and uniformly illuminated full-field (i.e., non-scanning) system for comparison. These lines correspond to the Rayleigh resolution limit and one definition of depth-of-focus, respectively.³¹

exploration of sub-Airy disk confocal pinholes in AO scanning light ophthalmoscopes (AOSLOs) by Zhang, Poonja, and Roorda,¹³ Merino et al.,²² Zou, Qi, and Burns,²³ and Dubra et al.²⁴ showed modest and hard to quantify improvements in transverse resolution. What follows is a study of the practical benefit of pursuing the sub-Airy disk confocal detection, motivated by the fact that, to the best of our knowledge, most current AOSLOs do not use pinholes smaller than 0.8 Airy disk diameter (ADD),²² thus not achieving the classical theoretical transverse resolution limit for a point-scanning instrument. Since the goal of this study is to evaluate image resolution, we chose to image the cone photoreceptor mosaic due to the point-like appearance of each individual cone-intensity profile.

Theory

A point-scanning confocal ophthalmoscope with AO is effectively a confocal microscope, enhanced with the optics of the eye playing the role of the microscope objective and the retina that of the sample. As a first approximation, the point-spread function (PSF) h of one such instrument free of wavefront aberrations is given by

$$h = |h_{\text{illumination}}|^2 \left(|h_{\text{imaging}}|^2 \otimes D \right), \quad (1)$$

where $h_{\text{illumination}}$ and h_{imaging} are the amplitude PSFs of the illumination and imaging arms, respectively; \otimes denotes convolution; and D is the spatial sensitivity

function of the light detector. The spatial sensitivity D is typically a binary function describing the transmission of the image conjugate confocal pinhole that precedes the light detector.⁹ In order to correctly interpret calculations derived from Eq. (1), it is important to be aware of the assumptions involved in its derivation, including (1) a point source producing uniform illumination at the pupil plane; (2) a small field of view, over which the illumination and imaging PSFs can be considered invariant; (3) a small numerical aperture so that scalar diffraction theory calculations and the Fraunhofer approximation are valid; and (4) an imaging process in which the interaction of the illumination light with the sample can be modeled as the product of the illumination and imaging intensity PSFs. This last point might not be valid due to the wave-guiding nature of their inner and outer segments.^{25,26} Therefore, it is not clear whether the Wilson and Carlini⁹ theory, developed for reflective and single-photon fluorescence samples,^{27–30} will correctly predict the potential improvement in resolution due to the use of sub-Airy disk detection.

Using Equation 1, the transverse and axial resolution of a microscope can be calculated as the full width at half maximum (FWHM) of the PSF at the focal plane and along the axis of propagation, respectively (left and center plots in Fig. 1). This equation also allows calculating the fraction of energy that would be collected by a finite size detector (Fig. 1, right plot). These curves show a potential improvement in transverse and axial resolution when

a detector smaller than the diameter of an Airy disk is used, at the cost of lower signal.

Methods

This work adhered to the tenets of the Declaration of Helsinki, and the institutional review boards of the Medical College of Wisconsin and Stanford University approved the study protocols. Five volunteers with no known ocular pathology were enrolled for this study. Pupils were dilated with 1 drop of 2.5% phenylephrine and 1 drop of 1% tropicamide prior to imaging. Artificial tear drops were administered whenever necessary. A bite bar attached to a three-axis translation stage was utilized to align and stabilize the subject's head.

Subject JC_10121 was imaged using two custom AOSLOs with 7.75 and 4.3 mm pupil diameters, henceforth referred to as the large- and small-pupil AOSLO, respectively.^{32,33} This study participant was imaged with two different AOSLOs to illustrate that the benefit of using sub-Airy disk detection is independent of the ophthalmoscope pupil diameter. The cone photoreceptor mosaic was imaged at the foveal center, defined as locus of fixation, with the large-pupil AOSLO and at 1° superior-temporal from fixation with the small-pupil AOSLO. The two locations were chosen to show the smallest cones resolvable by each instrument, and no comparison of image resolution is made between the instruments. Images were collected using confocal pinholes with the following sizes: 0.5, 0.6, 0.8, and 1.0 ADD. Four additional subjects were imaged with the large-pupil AOSLO using 0.5 and 1.0 ADD confocal pinholes to demonstrate that sub-Airy disk confocal imaging is viable in a population, rather than just in an exceptional subject.

Wavefront sensing was performed with an 850 nm superluminescent diode (Superlum, Carrigtwohill, Ireland) and a custom Shack-Hartmann wavefront sensor. Deformable mirrors (ALPAO, Montbonnot, France) with 97 actuators and an aperture diameter of 13.5 and 7.2 mm were used in the large- and small-pupil diameter AOSLOs, respectively. The retina was illuminated using a 790 nm superluminescent diode (Superlum), and the backscattered light was collected through a small confocal pinhole placed before an H7422-50 photomultiplier tube (PMT; Hamamatsu Photonics, Hamamatsu, Japan). The average incident power of the wavefront sensing and imaging sources measured at the cornea were 12 and 60 μW , respectively, for 0.75° (large-pupil AOSLO) and 1.5°

(small-pupil AOSLO), which we estimated to be at least five times below the American National Standards Institute maximum permissible exposure limit.³⁴

The pinhole alignment consisted of two steps. The first step was to focus the illumination by removing the confocal pinhole and to axially translate the tip of the optical fiber that provides illumination until maximum image sharpness/contrast was achieved when imaging a model eye consisting of an achromatic doublet and a piece of paper acting as a dummy retina following wavefront correction. This step was performed only once, as it is not pinhole dependent. In the second step, the confocal pinhole was placed in front of the detector on an xyz translation stage (ULTRAlign; Newport Corp., Irvine, CA) and moved in all three dimensions until the mean pixel value of the image was maximized. This method is highly repeatable in that it consistently delivers the same image mean pixel values for the same pinhole sizes. The distance between the pinhole and the light detector was adjusted to fill approximately 80% of the light-sensitive area of the detector to account for small potential misalignment.

Image sequences of 200 frames each, focused at the same depth in the retina, were collected at 16.7 Hz with the PMT gain adjusted to maintain constant mean pixel intensity across all experimental conditions. A stack of four image sequences was collected at each retinal location for each of the four pinhole sizes, with an estimated focus step between them of 3 μm for the large-pupil AOSLO and 6 μm for the small-pupil AOSLO. Thirty frames of each sequence were coregistered to compensate for distortion due to eye movement and averaged to improve signal-to-noise ratio.³⁵ The best focus was determined by subjectively identifying the sharpest registered average image from the stack that corresponded to the smallest confocal pinhole. The set of best focus images captured with all four pinhole sizes were then coarsely aligned using the "Reposition" option (translation only) using software (i2kAlign; Dual-Align LLC, Clifton Park, NY), followed by alignment with the bUnwarpJ plugin in Fiji (b-spline image registration).^{36,37} Finally, a logarithmic transformation of the grayscale was performed for better visualization of the cones. Image scale was determined through a model eye with a known focal length, scaled by the subject's ocular axial length measured with an optical biometry system (IOLMaster; Zeiss Meditec, Dublin, CA).³⁸

The images captured at the same retinal location

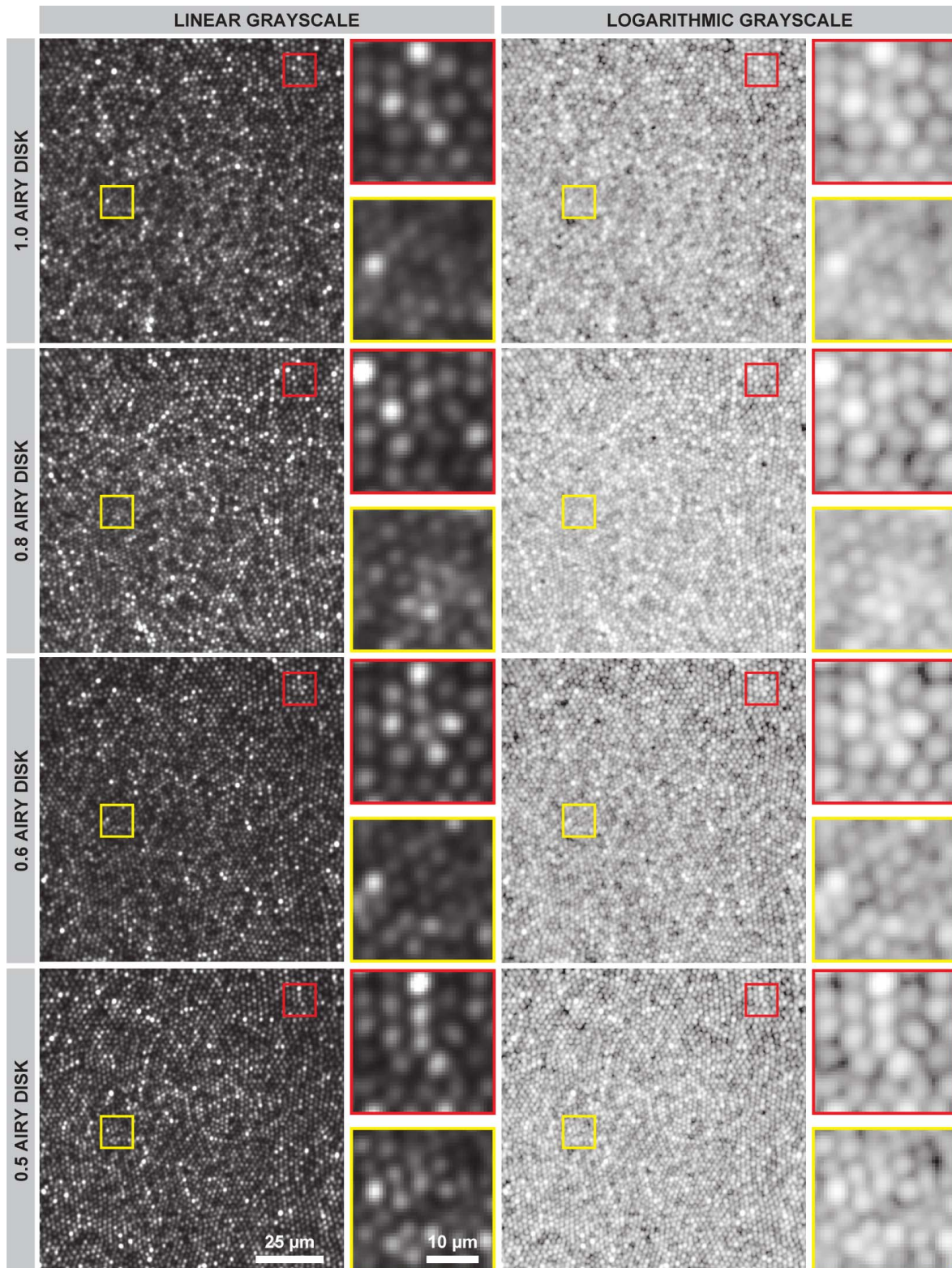


Figure 2. Images of the cone mosaic at the foveal center (fixation) of subject JC_10121 captured with a large-pupil AOSLO (7.75 mm at the eye) with various confocal pinhole sizes. The images are displayed on linear (*left*) and logarithmic (*right*) grayscales. The regions of interest enlarged in the *red* and *yellow inset boxes* are representative of the largest and smallest cones in the larger images, respectively.

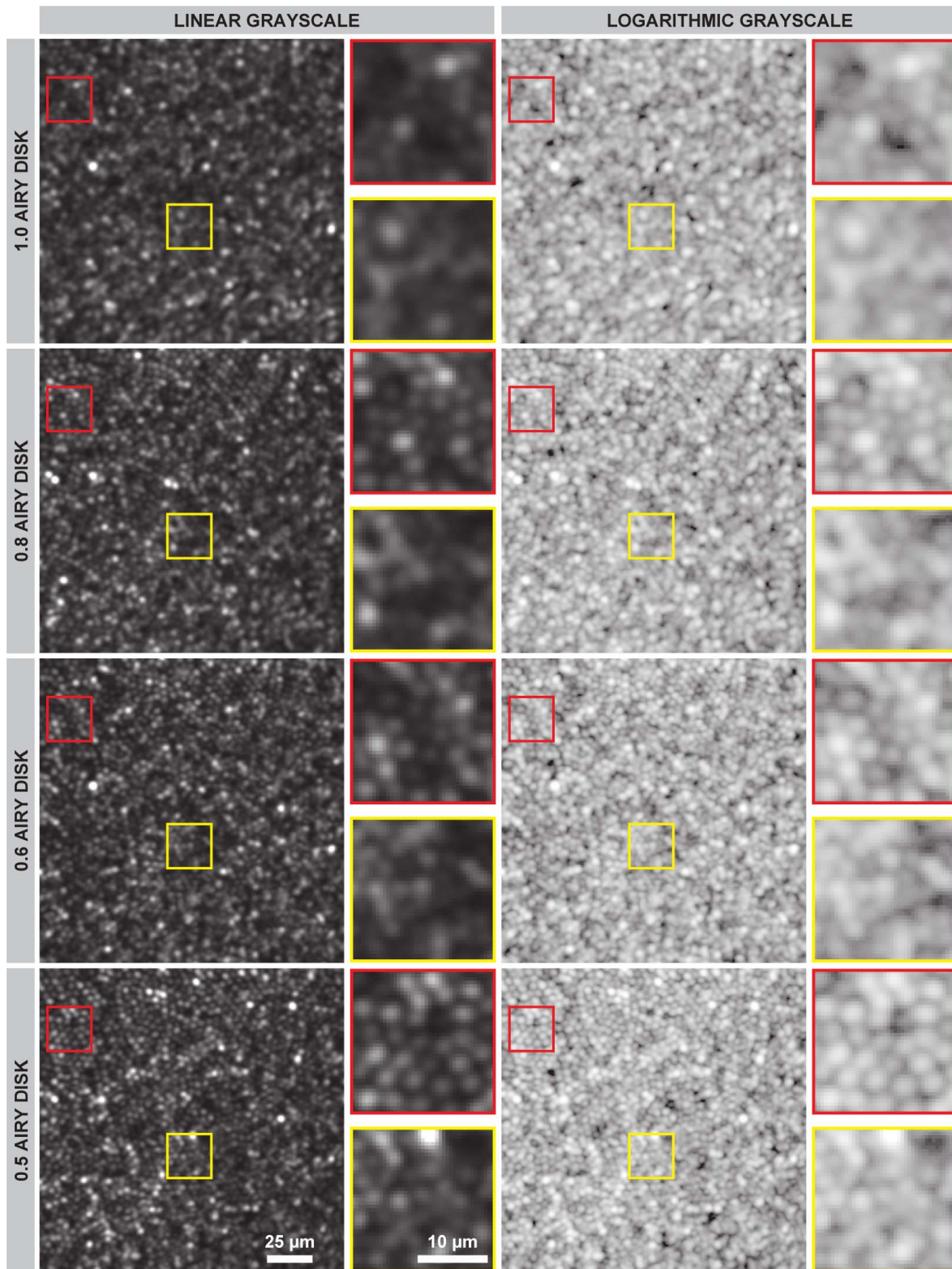


Figure 3. Images of the cone mosaic at 1° superior-temporal from the foveal center (fixation) of subject JC_10121 captured with a small-pupil AOSLO (4.3 mm at the eye) with various confocal pinhole sizes. The images are displayed on linear (*left*) and logarithmic (*right*) grayscale. The regions of interest enlarged in the *red* and *yellow inset boxes* are representative of the largest and smallest cones in the larger images, respectively.

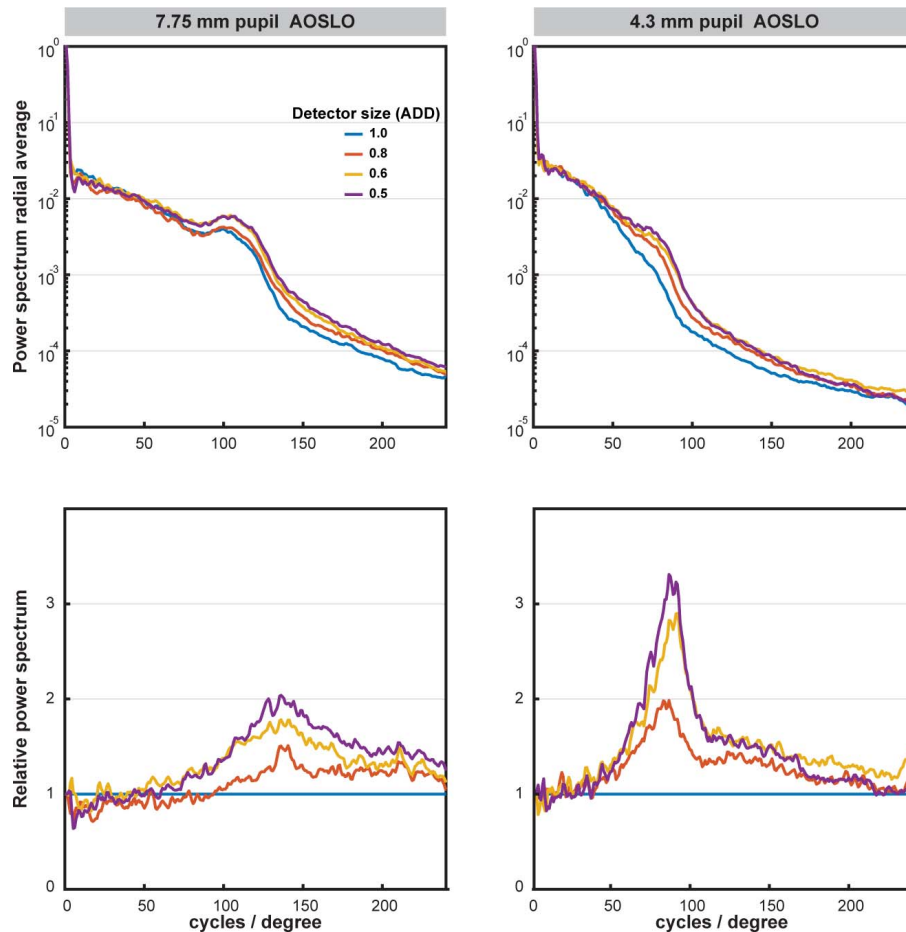


Figure 4. Absolute (*top*) and relative (*bottom*) radially averaged spectra of the retinal images captured with the large- and small-pupil AOSLOs shown in [Figures 2](#) and [3](#), with the higher spatial frequencies showing enhancement for the sub-Airy disk confocal pinholes in both instruments.

with different pinholes using the same instrument were compared with one another. The impact of decreasing pinhole size in the resulting images was evaluated through the radial average of the image spectra and the calculation of the average FWHM of the cones across each image. For the latter, each cone was first located at the position of its brightest pixel, and then the pixels above 50% of the peak value were identified and their circular equivalent areas used to estimate the cone FWHM. Only cones with their Voronoi cells fully contained within the images and with nonsaturated pixels were considered in these calculations.

Finally, the energy at the pinhole was measured using a model eye by placing a 1918-R power meter (Newport Corp.) after the pinhole. A model eye, rather than a human eye, was used to remove the variability due to eye motion, tear film evaporation, and other factors.

Results

The cone mosaic of subject JC_10121 can be better resolved with decreasing pinhole size in both the large- and small-pupil AOSLOs ([Figs. 2](#) and [3](#), respectively). The images corresponding to different

Table 1. Mean FWHM of Cone Photoreceptor Intensity Profiles (Linear Grayscale) in [Figures 2](#) and [3](#)

Confocal Pinhole Size, ADD	Cone FWHM, %	
	7.75-mm AOSLO	4.30-mm AOSLO
1.0	100	100
0.8	96	94
0.6	88	86
0.5	86	84

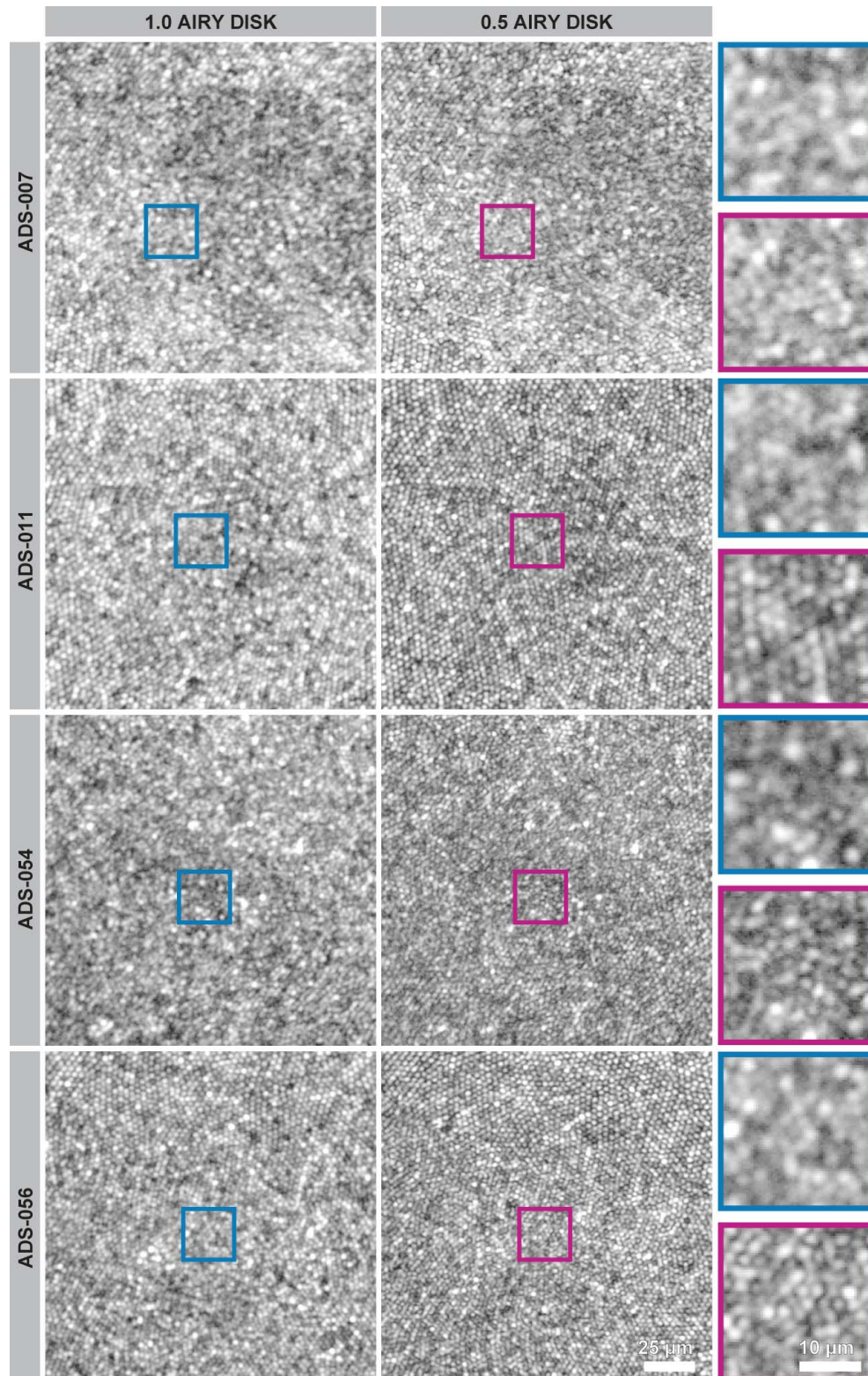


Figure 5. Images of the foveal cone mosaic (locus of fixation) of four healthy subjects captured with a 7.75 mm diameter pupil AOSLO with two different confocal pinholes (1.0 and 0.5 ADD). The images are displayed on a logarithmic grayscale. Representative magnified regions of interest indicated in the *blue* and *purple inset boxes* are provided to facilitate image comparison.

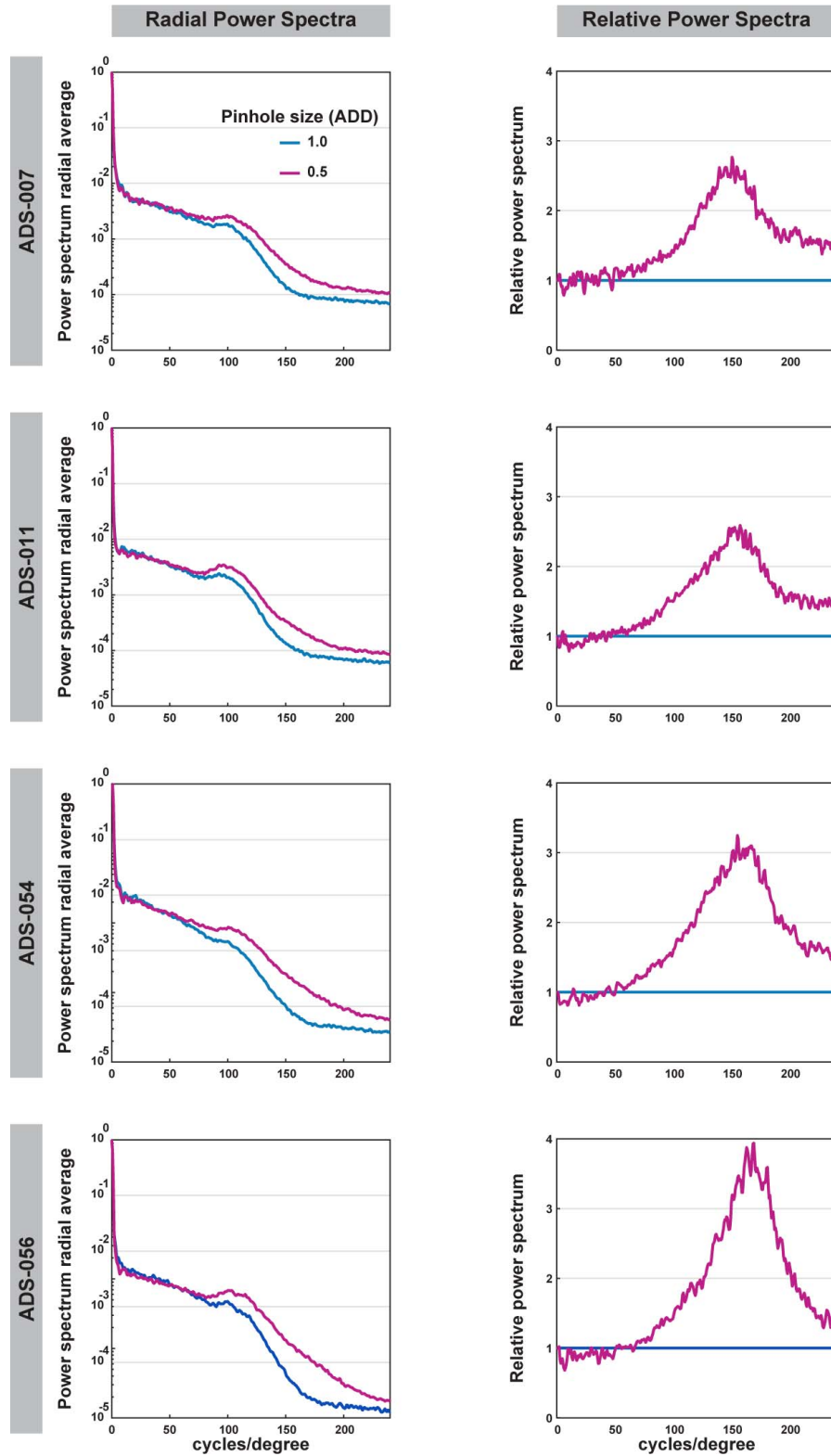


Figure 6. Absolute (left) and relative (right) radially averaged spectra of the retinal images from four healthy subjects captured with the large-pupil AOSLO shown in Figure 5, where a clear enhancement of the higher spatial frequencies can be seen with the use of 0.5 Airy disk confocal pinhole.

Table 2. Mean FWHM of Cone Photoreceptor Intensity Profiles (Linear Grayscale) in [Figure 5](#)

Subject ID	Cone FWHM, %	
	1.0 ADD	0.5 ADD
ADS_007	100	88
ADS_011	100	84
ADS_054	100	87
ADS_056	100	86

pinhole sizes were captured a few minutes apart, which makes the direct comparison of intensity challenging due to their well-documented normal intensity fluctuations.^{24,39} These intensity variations are evident when comparing the linear grayscale red and yellow insets that show enlarged regions of interest in [Figures 2](#) and [3](#). The logarithmic grayscale facilitates the comparison across pinhole sizes, mitigating the variability due to intensity fluctuations.

The radial average of the image power spectra ([Fig. 4](#)) shows substantial enhancement of high spatial frequencies when the pinhole size is reduced, particularly at the spatial frequencies that correspond to the average cone spacing in humans (~ 80 – 120 cycles/deg).⁴⁰

The average FWHM of the cone intensity profiles were reduced for all sub-Airy pinhole sizes and by 14

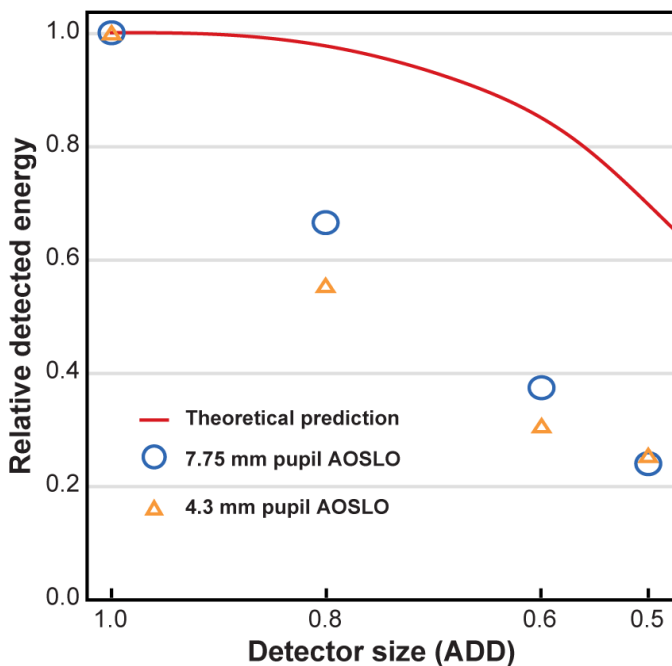
and 16% when the pinhole size was reduced by 50% in the large- and small-pupil AOSLOs, respectively ([Table 1](#)). The reduction in the FWHM is lower than predicted by theory ($\sim 20\%$; see [Fig. 1](#)). This is to be expected because the cones are not actually point sources (i.e., they have a finite size).

The images of the fovea, the radially averaged power spectra, and the reduction in FWHM of the cone intensity profiles from the additional four subjects imaged with the large-pupil AOSLO are shown in [Figure 5](#), [Figure 6](#), and [Table 2](#), respectively. The enhancement of the higher spatial-frequency content at 120 cycles/deg and the reduction in FWHM by $\sim 16\%$ with the use of a sub-Airy disk pinhole are consistent with the results seen in subject JC_10121. The improvement in the power spectrum with the use of sub-Airy disk pinholes, as seen in [Figure 4](#) and [Figure 6](#), is comparable to the improvement seen when using dynamic instead of static AO correction.⁴¹

Finally, the plot in [Figure 7](#) shows that the fraction of energy captured with the smaller pinholes as measured with a model eye is substantially lower than that predicted by theory. The large difference in predicted and measured reduction in signal intensity may be due to several factors. Non-common path aberrations between the illumination, imaging, and wavefront-sensing channels could contribute to blurred PSF.¹⁸ Because both AOSLOs use the same optical elements and configuration on the light sources, light detection, and wavefront-sensing arms of the optical setup, it seems logical that the data in [Figure 7](#) is consistent across instruments. Another contributing factor is likely the fact that the thickness of paper, acting as the retina in the model eye, is not negligible (~ 100 μm or ~ 0.28 diopters with a 19-mm lens).

Conclusions

The paraxial theory of linear confocal microscopy predicts an increase in transverse resolution with the use of sub-Airy disk confocal detection pinholes of up to 20% when using 0.5 ADD or smaller. The AOSLO imaging presented here shows that a substantial portion of this superior resolution is, in fact, attainable with current instruments despite several factors that are known to depart from the theoretical assumptions. These include finite light source size, imperfect ocular wavefront aberration correction, resonant scanner distortion that varies across the field of view, and wave-guiding properties

**Figure 7.** Theoretical and experimental energy at the confocal pinhole relative to a 1.0 ADD.

of the photoreceptors.^{25,26,42,43} If the observed reduction in signal is acceptable, the data presented here demonstrate that the use of a sub-Airy disk pinhole is a simple and practical method for improving image resolution in AOSLOs. Given the similarity of the imaging process, a comparable benefit should be expected in other point- and line-scanning ophthalmoscopes, such as optical coherence tomographers, irrespective of the retinal structure being imaged.

Acknowledgments

The authors thank Moataz M. Razeen at Stanford University, Christopher S. Langlo and Benjamin S. Sajdak at the Medical College of Wisconsin, as well as Drew Scoles at the University of Pennsylvania for assistance with manuscript preparation.

Supported by the Glaucoma Research Foundation Catalyst for a Cure Initiative, Research to Prevent Blindness Departmental Award (Stanford), and the National Eye Institute of the National Institutes of Health (NIH) under award numbers U01 EY025477 and R01 EY025231. The authors alone are responsible for the content and writing of the paper, which does not necessarily represent the official views of the National Institutes of Health.

Disclosure: **N. Sredar**, None; **O.E. Fagbemi**, None; **A. Dubra**, None

References

1. Webb RH, Hughes GW, Pomerantzeff O. Flying spot TV ophthalmoscope. *Appl Opt.* 1980;19:2991–2997.
2. Huang D, Swanson EA, Lin CP, et al. Optical coherence tomography. *Science.* 1991;254:1178–1181.
3. Elsner AE, Burns SA, Weiter JJ, Delori FC. Infrared imaging of sub-retinal structures in the human ocular fundus. *Vision Res.* 1996;36:191–205.
4. Norton HJJ. Absolute electronic retinal stereophotography. *Am J Ophthalmol.* 1955;40:809–817.
5. Donaldson DD. A new camera for stereoscopic fundus photography. *Trans Am Ophthalmol Soc.* 1964;62:429–458.
6. Talcott KE, Ratnam K, Sundquist S, et al. Longitudinal study of cone photoreceptors during retinal degeneration and in response to ciliary neurotrophic factor treatment. *Invest Ophthalmol Vis Sci.* 2011;52:2219–2226.
7. Webb RH, Hughes GW. Scanning laser ophthalmoscope. *IEEE Trans Biomed Eng.* 1981;28:488–492.
8. Webb RH, Hughes GW, Delori FC. Confocal scanning laser ophthalmoscope. *Appl Opt.* 1987;26:1492–1499.
9. Wilson T, Carlini AR. Size of the detector in confocal imaging systems. *Opt Lett.* 1987;12:227–229.
10. Roorda A, Romero-Borja F, Donnelly WJ 3rd, Queener H, Hebert T, Campbell M. Adaptive optics scanning laser ophthalmoscopy. *Opt Express.* 2002;10:405–412.
11. Hammer DX, Mujat M, Iftimia NV, Ferguson RD. Compact adaptive optics line scanning laser ophthalmoscope. *Proc SPIE.* 2009;7163.
12. Roorda A, Duncan JL. Adaptive optics ophthalmoscopy. *Annu Rev Vis Sci.* 2015;1:19–50.
13. Zhang Y, Poonja S, Roorda A. MEMS-based adaptive optics scanning laser ophthalmoscopy. *Opt Lett.* 2006;31:1268–1270.
14. Liu Z, Kocaoglu OP, Miller DT. In-the-plane design of an off-axis ophthalmic adaptive optics system using toroidal mirrors. *Biomed Opt Express.* 2013;4:3007–3030.
15. Ferguson RD, Zhong Z, Hammer DX, et al. Adaptive optics scanning laser ophthalmoscope with integrated wide-field retinal imaging and tracking. *J Opt Soc Am A.* 2010;27:A365–A277.
16. Hofer H, Sredar N, Queener H, Li C, Porter J. Wavefront sensorless adaptive optics ophthalmoscopy in the human eye. *Opt Express.* 2011;19:14160–14171.
17. Jian Y, Xu J, Gradowski MA, Bonora S, Zawadzki RJ, Sarunic MV. Wavefront sensorless adaptive optics optical coherence tomography for in vivo retinal imaging in mice. *Biomed Opt Express.* 2014;5:547–559.
18. Sulai Y, Dubra A. Non-common path aberration correction in an adaptive optics scanning ophthalmoscope. *Biomed Opt Express.* 2014;5:3059–3073.
19. Born M, Wolf E. *Principles of Optics.* 6th (corrected) ed. Oxford, UK: Pergamon Press; 1980.
20. Vohnsen B, Rativa D. Ultrasmall spot size scanning laser ophthalmoscopy. *Biomed Opt Express.* 2011;2:1597–1609.

21. Sulai YN, Dubra A. Adaptive optics scanning ophthalmoscopy with annular pupils. *Biomed Opt Express*. 2012;3:1647–1661.
22. Merino D, Duncan JL, Tiruveedhula P, Roorda A. Observation of cone and rod photoreceptors in normal subjects and patients using a new generation adaptive optics scanning laser ophthalmoscope. *Biomed Opt Express*. 2011;2:2189–2201.
23. Zou W, Qi X, Burns SA. Woofer-tweeter adaptive optics scanning laser ophthalmoscopic imaging based on Lagrange-multiplier damped least-squares algorithm. *Biomed Opt Express*. 2011;2:1986–2004.
24. Dubra A, Sulai Y, Norris JL, et al. Noninvasive imaging of the human rod photoreceptor mosaic using a confocal adaptive optics scanning ophthalmoscope. *Biomed Opt Express*. 2011;2:1864–1876.
25. Gao W, Cense B, Zhang Y, Jonnal RS, Miller DT. Measuring retinal contributions to the optical Stiles-Crawford effect with optical coherence tomography. *Opt Express*. 2008;16:6486–6501.
26. Roorda A, Williams DR. Optical fiber properties of individual human cones. *J Vis*. 2002;2:404–412.
27. Wilson T, Sheppard C. *Theory and Practice of Scanning Optical Microscopy*. London: Academic Press; 1984.
28. Kimura S, Munakata C. Calculation of three-dimensional optical transfer function for a confocal scanning fluorescent microscope. *J Opt Soc Am A*. 1989;6:1015–1019.
29. Gu M, Sheppard C. Confocal fluorescent microscopy with a finite-sized circular detector. *J Opt Soc Am A*. 1992;9:151–153.
30. Gu M, Sheppard C. Comparison of three-dimensional imaging properties between two-photon and single-photon fluorescence microscopy. *J Microsc*. 1995;177:128–137.
31. Rayleigh L. Investigations in optics, with special reference to the spectroscope. *Lond Edinb Dubl Phil Mag*. 1879;8:261–274.
32. Dubra A, Sulai Y. Reflective afocal broadband adaptive optics scanning ophthalmoscope. *Biomed Opt Express*. 2011;2:1757–1768.
33. Sredar N, Razeen MM, Sulai YNB, Sajdak BS, Dubra A. Non-confocal split-detection adaptive optics scanning light ophthalmoscope with small pupil for vascular imaging. *Invest Ophthalmol Vis Sci*. 2016;57:62–62.
34. Delori FC, Webb RH, Sliney DH. Maximum permissible exposures for ocular safety (ANSI 2000), with emphasis on ophthalmic devices. *J Opt Soc Am A*. 2007;24:1250–1265.
35. Dubra A, Harvey Z. Registration of 2D images from fast scanning ophthalmic instruments. In: Fischer B, Dawant B, Lorenz C, eds. *Biomedical Image Registration*. Berlin: Springer-Verlag; 2010: 60–71.
36. Schindelin J, Arganda-Carreras I, Frise E, et al. Fiji: An open-source platform for biological-image analysis. *Nat Methods*. 2012;9:676–682.
37. Arganda-Carreras I, Sorzano COS, Marabini R, Carazo JM, Ortiz-de-Solorzano C, Kybic J. Consistent and elastic registration of histological sections using vector-spline regularization. In: Beichel RR, Sonka M, eds. *Computer Vision Approaches to Medical Image Analysis*. Berlin: Springer; 2006:85–95.
38. Li KY, Tiruveedhula P, Roorda A. Intersubject variability of foveal cone photoreceptor density in relation to eye length. *Invest Ophthalmol Vis Sci*. 2010;51:6858–6867.
39. Cooper RF, Dubis AM, Pavaskar A, Rha J, Dubra A, Carroll J. Spatial and temporal variation of rod photoreceptor reflectance in the human retina. *Biomed Opt Express*. 2011;2:2577–2589.
40. Curcio CA, Sloan KR, Kalina RE, Hendrickson AE. Human photoreceptor topography. *J Comp Neurol*. 1990;292:497–523.
41. Hofer H, Chen L, Yoon GY, Singer B, Yamauchi Y, Williams DR. Improvement in retinal image quality with dynamic correction of the eye's aberrations. *Opt Express*. 2001;8:631–643.
42. Stiles WS, Crawford BH. The luminous efficiency of rays entering the eye pupil at different points. *Proc R Soc Lond B*. 1933;112:428–450.
43. Snyder AW, Pask C. The Stiles-Crawford effect—explanations and consequences. *Vis Res*. 1973;13: 1115–1137.